PHYSICAL REVIEW B **81**, 235317 (2010)

Photoluminescence from silicon dioxide photonic crystal cavities with embedded silicon nanocrystals

Yiyang Gong,[1,*] Satoshi Ishikawa,[2] Szu-Lin Cheng,[3] Marika Gunji,[3] Yoshio Nishi,[1] and Jelena Vučković[1]
[1]*Department of Electrical Engineering, Stanford University, Stanford, California 94305, USA*
[2]*Corporate Manufacturing Engineering Center, Toshiba Corporation, Yokohama 235-0017, Japan*
[3]*Department of Material Science and Engineering, Stanford University, Stanford, California 94305, USA*

(Received 27 February 2010; revised manuscript received 10 May 2010; published 14 June 2010)

One-dimensional nanobeam photonic crystal cavities are fabricated in silicon dioxide with silicon nanocrystals. Quality factors of over 9×10^3 are found in experiment, matching theoretical predictions, with mode volumes of $1.5(\lambda/n)^3$. Photoluminescence from the cavity modes is observed in the visible wavelength range 600–820 nm. Studies of the lossy characteristics of the cavities are conducted at varying temperatures and pump powers. Free carrier absorption effects are found to be significant at pump powers as low as a few hundred nanowatts.

DOI: 10.1103/PhysRevB.81.235317 PACS number(s): 42.60.Da, 42.72.Bj, 78.67.Bf

The promise of integrating electronics and optics has fueled the search for efficient light-emitting materials compatible with silicon complementary metal-oxide-semiconductor (CMOS) processing. The system of silicon nanocrystals (Si-NCs) embedded in a silicon dioxide (SiO_2, or silica) host has been proposed as one such candidate, capable of emitting in the visible and near-infrared wavelengths and possibly exhibiting gain.[1,2] While the quantum-confinement properties of the material relax some constraints for radiative recombination in the indirect band-gap silicon, the efficiency of this material is still low. The photonic crystal (PC) cavity system, with high quality (Q) factor and low-mode volume (V_m), could enhance radiative emission from the nanocrystals via Purcell enhancement of the radiative rate, which is proportional to Q/V_m. By enhancing the radiative rate with respect to the nonradiative decay rates, the efficiency of the Si-NC emission can be increased. In addition, the high-Q cavity could be used to spectrally filter signals and define operating wavelengths from the broad luminescence range of the Si-NCs. The lossy mechanisms of this material coupled to microdisks (μ-disks) were previously analyzed,[3,4] and it was noted that free carrier absorption (FCA) may play a significant role in lossy processes and may ultimately inhibit gain in this material.[4] In addition, lossy mechanisms were also studied in ultrahigh Q bottle resonators, which have relatively large V_m.[5] In this work, we demonstrate Si-NCs embedded in a silicon dioxide host coupled to high Q and low V_m PC nanobeam cavities, fabricated by CMOS compatible processing. In addition, we investigate the temperature and pump power dependence of the cavities, and compare them to previous work. We observe that free carrier absorption remains significant in high-Q and low-V_m photonic crystal cavities, and is even present at very low pump powers of a few hundred nanowatts.

Si-NCs can be grown in a SiO_2 host by either Si implantation[2] or plasma-enhanced chemical-vapor deposition (PECVD). One of the previous hindrances to producing high-Q PC cavities was the small optical band gap afforded by low index materials in a two-dimensional (2D) PC setting. For example, Barth *et al.* were able to experimentally demonstrate $Q=3400$ in silicon nitride (Si_3N_4) (Ref. 6) with a heterostructure two-dimensional PC cavity in a triangular lattice. While a full photonic band gap in a 2D photonic crystal is difficult to achieve in low index materials, one-dimensional (1D) nanobeam cavities that rely on a one-dimensional band gap in the direction parallel to the beam and total internal reflection in the remaining two directions perpendicular to the beam can lead to high-Q factors with low index contrast. Recent work has found that such a design can be applied to materials with a variety of indices of refraction, including Si ($n=3.5$),[7,8] Si_3N_4 ($n=2.0$),[9,10] and even SiO_2 ($n=1.46$).[11] In particular, the experimentally demonstrated Q's exceed 10^5 for Si,[8] 10^4 for Si_3N_4,[9] and 10^3 for SiO_2 (Ref. 11) while maintaining $V_m<2.0(\lambda/n)^3$.

We employ the parabolic potential well design of previous works,[9,11] where the distance between air holes on the beam increases parabolically from the center of the beam outward. The cavity extends six air holes on either side of the center of the cavity, where the distance between air holes is $0.9a$ at the center of the cavity, while holes outside of the cavity in the photonic crystal mirror have with lattice constant a. The beam has width (w) and thickness (d) while the air holes on the beam have horizontal size ($h_x=0.5a$) and vertical size ($h_y=0.7w$) [Fig. 1(a)]. We simulate the cavity using the three-dimensional finite difference time domain (FDTD) method, with a discretization of 20 units per lattice constant and apply perfectly matched layer absorbing boundary conditions. For a cavity with $d/a=0.7$ and $w/a=3.2$, and assuming the Si-NC-doped oxide material to have an index of refraction of $n=1.7$, we find that the cavity supports at least three transverse electric- (TE-) like modes, which have dominant E_y field profiles shown in Figs. 1(b)–1(d), and are referred to as the first- (TE_0, or fundamental), second- (TE_1), and third-order (TE_2) modes, respectively.[12] The TE_0, TE_1, and TE_2 modes have normalized mode frequencies of $a/\lambda=0.417$, 0.398, and 0.385, respectively, with the electric field energy of higher-order modes occupying regions on the beam with increasing lattice constants. In addition, we compute the Q of the cavity as $Q=\omega U/P$, where ω is the frequency of the mode, U is the total energy of the mode, and P is the time-averaged radiated power. We find that the TE_0, TE_1, and TE_2 modes have radiation limited Q's of 2.0

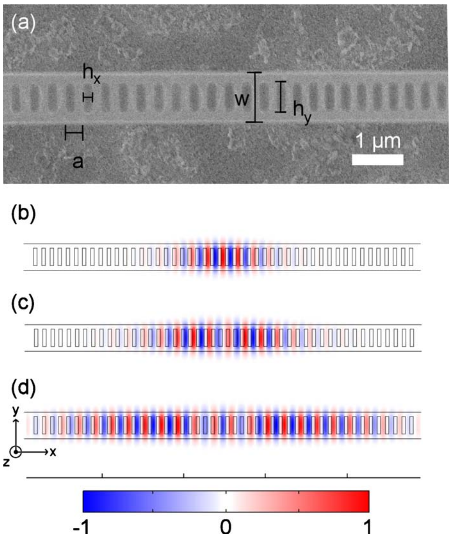

FIG. 1. (Color online) (a) SEM picture of the fabricated beam structure. The E_y component of the (b) first- (c) second-, and (d) third-order TE-like modes supported by the nanobeam with parameters $w=3.2a$, $h_x=0.5a$, $h_y=0.7w$, and thickness $d=0.7a$ are also shown.

$\times 10^4$, 1.3×10^4, and 2.9×10^3, and mode volumes of $1.6(\lambda/n)^3$, $2.5(\lambda/n)^3$, and $4.4(\lambda/n)^3$, respectively, for a reference index of $n=1.7$.

We also vary the width (w) and thickness (d) of the beam with the same fixed air hole design, and find Q and V_m for different beam parameters, Figs. 2(a) and 2(b), respectively. For $w<2.4a$, we find that the confinement of the mode (and thus the Q) increases as the beam increases in either width or thickness and that the V_m correspondingly increases. Such a trade-off between Q and V_m was previously observed in silica nanobeam cavities,[11] and is also present in other types of cavities, including 2D PC cavities and μ-disk systems. In addition, we observe that for all beam widths, such a trade-off is maintained as the thickness of the beam is increased. However, we see that the Q of the cavity mode saturates as the width of the beam is increased beyond $w>2.4a$, as confinement of the mode in the y direction is no longer dominant in the overall confinement of the mode. Indeed, the thicknesses (d) of the beams are far smaller than the width at $w=2.4a$ and increasing d further increases confinement. Likewise, the k-space emission profile could remain largely unchanged by the increase in the beam width thus limiting the Q achieved by this air hole design. In the future, modifications to the air hole design could increase the Q's for this type of cavity. In order to maximize the Purcell enhancement for this cavity, we would maximize the Q/V_m ratio, which (in this parameter space), is achieved at $w=1.6a$ and $d=1.1a$, corresponding to radiation limited $Q=25\,000$ and $V_m=1.1(\lambda/n)^3$. This represents an order of magnitude increase in Q and seven times reduction in mode volume compared to μ-disks with a similar thickness and a diameter of 5 μm.[3]

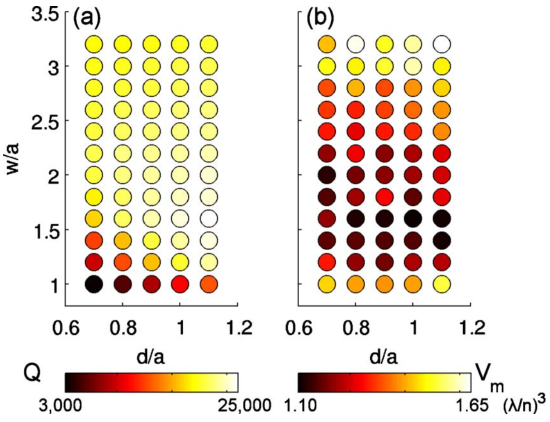

FIG. 2. (Color online) (a) Q and (b) V_m for the TE_0 mode for different beam widths (w) and thicknesses (d). We keep the same air hole design for the simulated cavities.

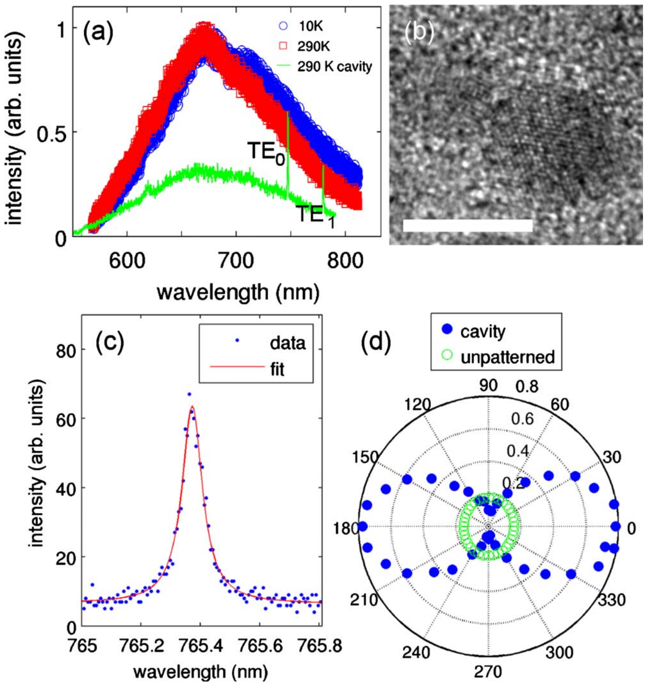

FIG. 3. (Color online) (a) PL spectra from unpatterned film at 10 and 290 K, as well as a cavity spectrum at 290 K with the first two TE modes visible. (b) TEM image of representative Si-NCs. The scale bar represents 5 nm. (c) The PL spectrum of a representative fundamental cavity mode at 290 K and the fit to a Lorentzian with $Q=9000$. (d) The polarization angle dependence of the cavity mode at 290 K along with the angle dependence of PL from an unpatterned region. 0° corresponds to the y direction of Fig. 1(d).

The cavities are fabricated by a fully CMOS compatible process with similar parameters as in simulations. In particular, the Si-NC-doped oxide layer is grown on top of a silicon substrate by PECVD at 350 °C in a N_2 atmosphere with a gas flow of $SiH_4:N_2O=1400:300$ sccm. The growth rate is approximately 46 nm/min and the final oxide thickness is 200 nm. The sample is then annealed in a N_2 atmosphere at 900 °C for 1 h, followed by a forming gas (95% N_2, 5% H_2) anneal at 500 °C for 1 h. A transmission electron microscope (TEM) image of representative Si-NCs are shown in Fig. 3(b). The refractive index of the layer is measured as $n=1.7$ at 700 nm by ellipsometry. Next, e-beam lithography is performed with a 250-nm layer of ZEP-520A as the resist. After development of the resist, the pattern is transferred to the oxide layer with a $CHF_3:O_2$ (100 sccm/2 sccm ratio) chemistry dry etch.[11] Finally, the beam is undercut with a 1.0 Torr XeF_2 dry etch, removing approximately 3 μm of silicon under the oxide layer. The final fabricated structure is shown in Fig. 1(a). We vary the lattice constant a in fabrication to create cavities with a variety of wavelengths, where all beams have a width of $w=3.2a$ (due to fabrication constraints).

The microphotoluminescence (μ-PL) experiments are conducted with a 75× objective lens with numerical aperture NA=0.75, focusing the pump to a 3-μm diameter spot. The sample is pumped from normal incidence (z) with either a continuous-wave (CW) 400 nm laser diode or a frequency doubled Ti:Sapphire laser at 390 nm with 3 ps pulses at 80 MHz. The photoluminescence is also collected from normal incidence through the same objective and directed to a Si charge-coupled-device array in a spectrometer with resolution of 0.01 nm. The cryogenic temperature experiments are conducted in a helium flow cryostat with temperatures as low as 5 K. Room temperature data was taken outside of vacuum. We observe the PL from an unpatterned region of the sample at both 10 and 290 K, using the 400 nm CW laser as the pump [Fig. 3(a)]. The PL spectrum is centered at around 670 nm, and is the same at both temperatures, which suggests that the change in the homogeneous linewidth for the Si-NCs is small with temperature. Finally, we observe that the PL of the sample pumped with the pulsed Ti:Sapph laser (not shown) was the same as the PL in Fig. 3(a) at both temperatures, similar to previous work.[13]

We also investigate the cavities in the same μ-PL configuration, first at room temperature. A representative cavity spectrum at 290 K is shown in Fig. 3(a), where at least the first two orders of TE modes (TE$_0$ and TE$_1$) are visible. We also plot the spectrum of the fundamental mode of a high-Q cavity along with a fit to a Lorentzian lineshape, representing $Q=9000$, in Fig. 3(c). Finally, we measure the polarization angle dependence of the cavity mode by placing a polarizer and a half wave plate in the PL collection path, plotted in Fig. 3(d). The cavity mode is dominated by the E_y field and the mode is measured to have a linear polarization in the y direction. On the other hand, the PL collected from the unpatterned region is unpolarized. As seen from the FDTD simulations, the TE$_0$ mode has the highest Q and lowest V_m. Thus, we choose to work with the fundamental mode for the remainder of this work to maximize the Purcell effect.

We measure the Q factors of various cavities throughout the Si-NC PL spectrum at temperatures between room temperatures and 5 K, as shown in Fig. 4(a). The cavities are all pumped with the CW diode laser at very low pump powers (200 nW), which is necessary to reduce the cavity losses stemming from FCA. The different cavities have different lattice constant a, but have the same fixed $w/a=3.2$ ratio, $d=200$ nm, and the same air hole design. We find that for all cavities, the cavity Q continuously drops to approximately one half of the room-temperature value at 5 K. Such change in cavity Q can be attributed to the difference in the homogeneous linewidth of the Si-NCs at the two temperatures. As seen in previous work on coupling Er emission to PC cavities, the Purcell enhancement of absorption is degraded when the homogeneous linewidth of the emitter far exceeds that of the cavity linewidth.[14] Single Si-NCs have measured linewidths of over 100 nm at room temperature but have far narrower linewidths down to 1 nm at 35 K.[15] Thus, the narrower linewidth at low temperature increases the absorption of the Si-NCs coupled to the cavity mode and lowers the Q of the cavities. The temperature dependence of Q suggests that the homogeneous linewidth of the Si-NCs continuously decreases with temperature, much as in previous work.[15]

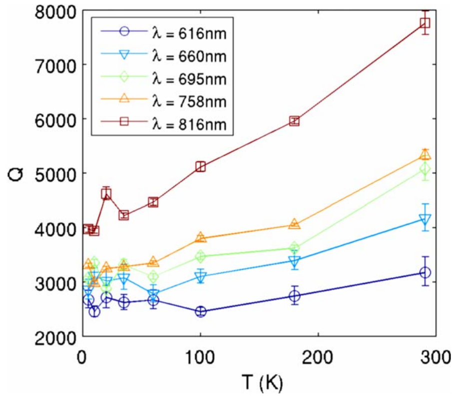

FIG. 4. (Color online) The Q's of cavities at different wavelengths as a function of temperature.

In addition, we study the Q's of many cavities at the extremes of the temperature at 10 K and room temperature, where the same set of cavities was measured at both temperatures [Fig. 5(a)]. We again notice that the Q's of the cavities are higher at room temperature than the Q's of the same cavities at 10 K. Because the lattice constant increases for the longer wavelength cavities, the d/a ratio decreases with increasing cavity wavelength. We note in Figs. 4(a) and 5(a) that the cavities have increasing Q at longer wavelengths, which disagrees with the simulated trend of higher

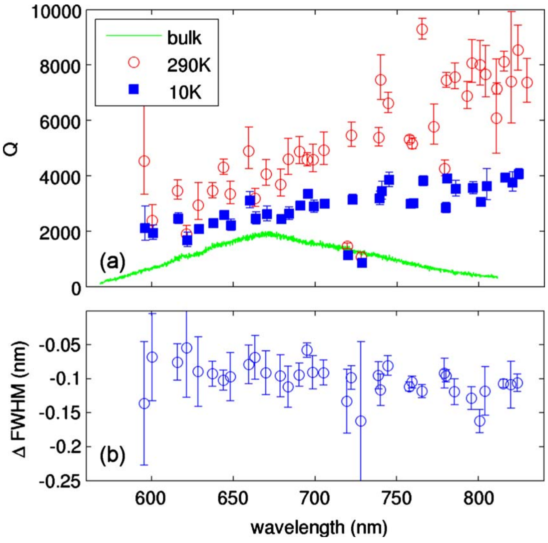

FIG. 5. (Color online) (a) The Q's of the one set of cavities vs the cavity wavelengths, at 10 and 290 K. The PL from an unpatterned region of the sample is shown for reference. (b) The change in the cavity linewidth as the temperature is increased from 10 to 290 K.

Q's for thicker beams (higher d/a). While this discrepancy could be caused by higher sensitivity to surface roughness for cavities operating at shorter wavelengths, we do not observe this effect in similar cavities made in pure SiO_2.[11] Thus, we attribute the decreasing Q with decreasing lattice constant to the material absorption of the Si-NCs, which increases with decreasing wavelength (as more NCs contribute to absorption). We also measure the change in the cavity linewidth for the same set of cavities between 290 and 10 K, shown in Fig. 5(b). We notice that the decrease in the linewidth with increasing temperature is approximately uniform and equal to 0.10–0.15 nm for the entire wavelength range of the Si-NC PL. The losses in the cavity can be related to the cavity Q by

$$\frac{\omega}{Q} = \frac{\omega}{Q_0} + \gamma(T,P), \tag{1}$$

where ω is the cavity frequency, Q_0 is the intrinsic cavity Q, and $\gamma(T,P)$ is the pump power and temperature-dependent loss rate. The intrinsic Q change with temperature is negligible, as a result of the small change in refractive index [as can be concluded from the negligible change in cavity wavelength shift with temperature, shown in Fig. 4(b)]. In this case, the measured linewidth difference is the change in $\gamma(T,P)$ with temperature and suggests that the linewidth narrowing of the Si-NCs is uniform throughout the PL spectrum.

We also use 10 and 290 K as representative temperatures for measuring the power dependence of the cavities. We employ both the CW diode laser and the pulsed doubled Ti:Sapphire laser in the power dependence studies, and we pump various representative cavities throughout the PL wavelength range. By fitting the obtained spectra to Lorentzian lineshapes, we obtain the integrated emission, cavity wavelength, and cavity linewidth. In Figs. 6(a) and 6(b), we first investigate the integrated cavity intensity obtained from the fits at 290 K and 10 K, respectively, as a function of pump power. We observe that the cavity output is approximately linear in the pump power, with some slight sublinear characteristics, mostly likely due to FCA. In addition, we find that at both temperatures, the output for the pulsed pump generates slightly more PL. Finally, at room temperature, the output intensities of the cavities have slightly lower slope for the pulsed pump than for the CW pump. On the other hand, the slopes of the light-in light-out curves are approximately the same for the different types of pump at 10 K. Such sublinear behavior at small pump powers is similar to the trend from previous work with Si-NCs coupled to μ-disk cavity modes.[4] The smaller increases in the cavity amplitude with increasing pump power for pulsed pumping suggest that lossy mechanisms are more readily found with pulses and high instantaneous pump intensities.

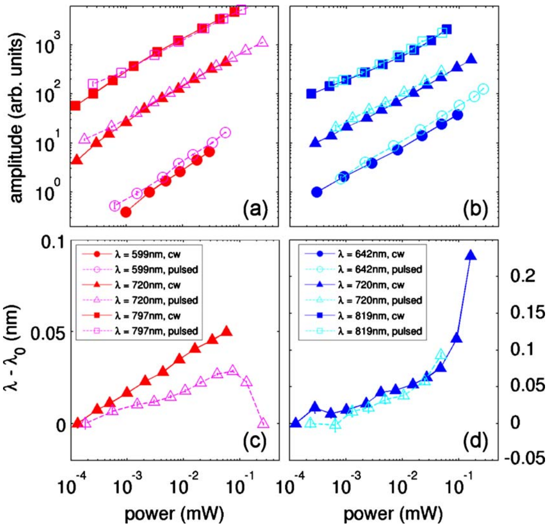

FIG. 6. (Color online) The pump power dependence of the integrated intensity for different cavities at (a) 290 K and (b) 10 K. The amplitude traces of each cavity are offset by factors of 10 to allow clear viewing. The pump power dependence of the change in cavity wavelength (with respect to the low pump power wavelength, λ_0) for different cavities at (c) 290 K and (d) 10 K. Power dependences were taken with both the CW diode laser and the pulsed frequency-doubled Ti:Sapphire. The pump power is measured in front of the objective.

We also find the pump dependence of the change in the cavity wavelength from the fits to a Lorentzian lineshape, and plot the results for the cavities around 720 nm in Figs. 6(c) and 6(d), obtained at 290 K and 10 K, respectively. We observe that in both cases, the cavity continuously redshifts with increasing pump power, implying the thermal-optic effect as the cause.[4] At room temperature, the pulsed pump generates far less heating than the CW pump, while at 10 K, the wavelength shifts are approximately the same between the two pump methods. In addition, at high pump powers for both CW and pulsed pumping, we observe melting of the cavities, where the wavelength of the cavities abruptly blueshifts [e.g., in Fig. 6(c) for the pulsed pumping]. In order to avoid this regime, pump powers are kept below 500 μW for all experiments. We also note that the wavelength shift for the cavities can be related to the index of refraction change caused by the thermal-optic effect by (using the perturbation method of Ref. 16)

$$\Delta\lambda \approx \lambda \frac{\Gamma}{2} \frac{\Delta\epsilon}{\epsilon}, \tag{2}$$

where Γ is the fraction of the mode overlapping with the Si-NC-doped oxide, λ is the unperturbed cavity wavelength, $\Delta\lambda$ is the change in cavity wavelength, $\Delta\epsilon$ is the change in dielectric constant, and ϵ is the dielectric constant of the Si-NC-doped oxide. For the TE_0 cavity mode at 720 nm, we obtain $\Gamma = 0.52$ from FDTD simulations, and find that the index of refraction shift is $\Delta n = 2.2 \times 10^{-4}$, which corresponds to a temperature change of 20 K, using the bulk thermal-optic coefficient of oxide, $dn/dT = 1 \times 10^{-5}/\text{K}$. Such a change in index (and temperature) is achieved with approximately two orders of magnitude less power than in the μ-disk setting.[4] This large change is due to the lack of heat conduction from the nanobeam cavities, as noted from previous work with thermal-optical bistability in 1D nanobeam cavities fabricated in silicon.[17] The changes in index with temperature are doubled when pumping the cavities at 10 K, possibly due to reduced air convection inside a vacuum.

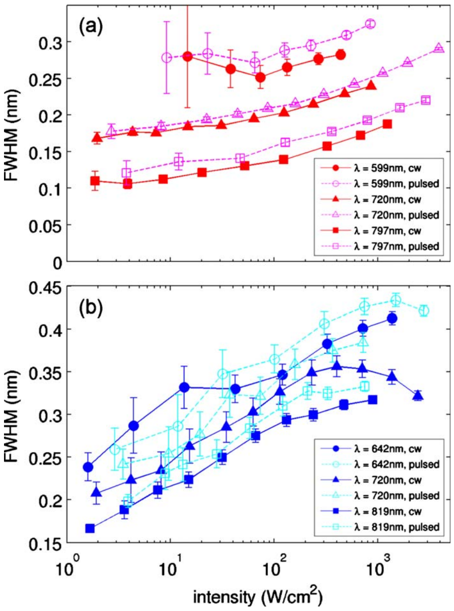

FIG. 7. (Color online) The linewidths of representative cavities as the pump power is changed at (a) 290 K and (b) 10 K. Both a CW diode laser and a frequency doubled mode-locked Ti:Sapphire laser are used as the pump source. The pump power is measured in front of the objective.

Finally, we measure the cavity linewidth for representative cavities throughout the Si-NC PL spectrum, at both 290 K and 10 K in Figs. 7(a) and 7(b), respectively. We note that the cavity linewidth continuously increases with increasing pump power, regardless of cavity wavelength or cavity Q. The linewidth data resembles the linewidth data for μ-disk modes in Ref. 4, though the low pump power Q's for the nanobeam cavities are approximately four to eight times higher. Broadening of the cavity linewidth is thought to be resulting from FCA. We find that the power necessary to observe FCA is more than an order of magnitude less than in the μ disks,[4] corresponding to a pump flux of 3 W/cm^2. Following the slope of the curves in Fig. 7, smaller powers could also generate losses from free carrier absorption. As described previously,[4] the onset of FCA only occurs when the FCA dominates other processes such as Mie scattering and band-to-band absorption in nanocrystals. On the other hand, in high-Q, low-V_m systems, we observe that free-carrier absorption dominates the other processes, and that linewidth broadening effect from FCA occurs at even small powers. In addition, the linewidth increases until at high pump powers (>100 μW), there is a sudden increase due to overheating and melting of the cavities. In previous work, the losses arising from FCA in μ-disks were saturated when the carrier density is sufficiently high to promote Auger recombination.[4] However, we do not reach that regime, as the pump intensities required are higher than that to destroy the cavities. We further note that the cavity linewidth for each cavity is narrower with the CW pump than with the pulsed pump at room temperature. Such evidence corroborates the conclusion that pulsed pumping induces more losses in the cavities than CW pumping.

We attempt to characterize the FCA mechanism following the procedure in Ref. 4. First, we find the distribution of Si-NC sizes by assuming that the energy of emission for the Si-NCs is related to the size of the NCs by[4,18]

$$\hbar\omega = E_{g,\mathrm{Si}} + \frac{3.73}{(2R)^{1.39}}, \tag{3}$$

where $E_{g,\mathrm{Si}}=1.12$ eV is the band-gap energy of bulk Si, $\hbar\omega$ is the energy of emission in eV, and R is the radius of the NC in nanometers. The emission at each energy is proportional to the density of nanocrystals at a particular size, and the proportionality constant is found by finding the volume ratio of Si in the entire film, assuming complete phase segregation. By finding the mass fractions of Si ($x_{\mathrm{Si}}=0.42$) and O ($x_{\mathrm{O}}=0.47$) obtained from x-ray photoelectron spectroscopy, we find that the distribution of nanocrystal sizes $[\rho(R)]$ as the distribution shown in Fig. 8(a). As expected, the distribution of NCs has smaller radii than the NCs of Ref. 4, as the NC emission has been pushed to shorter wavelengths. By integrating the distribution for all radii, we find a total nanocrystal density of $N_{NC}=7\times10^{18}$ cm^{-3}, which is comparable to the densities obtained in other works.[2,4]

We also find the pump power dependent rise (τ_r) and fall (τ_f) times of the Si-NCs, by chopping the CW diode pump with an acousto-optic modulator with 15 ns rise and fall times. Representative time traces from unpatterned regions of the sample can be found in Fig. 8(b), for the sample at 290 and 10 K. Stretched-exponential functions are fitted to the data to find τ_r and τ_f.[19] The τ_f of the sample is found to be approximately 20 μs at 290 K and approximately 80 μs at 10 K [Fig. 8(c)]. The longer lifetime at low temperatures is expected, as similar samples of porous silicon also demonstrate a dramatic increase in lifetime with decreasing temperature, which was attributed to longer radiative lifetimes and higher fraction of the emission coming from the diffusion of carriers.[19] It is also possible that nonradiative recombination centers and recombination at daggling bonds is reduced with temperature. The excitation cross section of the Si-NCs at a particular wavelength λ $[\sigma_{ex}(\lambda)]$ can be related to τ_r, τ_f, and the pump flux ϕ by[4]

$$\frac{1}{\tau_r(\lambda)} = \sigma_{ex}(\lambda)\phi + \frac{1}{\tau_f(\lambda)}. \tag{4}$$

By conducting time-resolved measurements at various wavelengths, using 10-nm band-pass filters to spectrally filter the emission, we find σ_{ex} by a linear fit of the pump-flux-dependent difference of $1/\tau_r - 1/\tau_f$ to ϕ with the results shown in Fig. 8(c). Finally, the occupation (the number of electron-hole pairs) of individual Si-NCs at a particular size and pump flux $[f(R,\phi)]$ is found by the relation[4]

$$\frac{\sigma_{ex}(\lambda)\phi}{\hbar\omega_p} - \frac{f(R,\phi)}{\tau_f(\lambda)} - \frac{f^3(R,\phi)}{\tau_A(\lambda)} = 0, \tag{5}$$

where ω_p is the pump laser frequency and τ_A is the Auger recombination time. The Auger time constant can be found by $\tau_A = 1/C_A \times (V/2)^2$, where $C_A = 4\times10^{-31}$ cm^6/s is the Auger recombination coefficient for bulk Si, and V is the volume of the Si-NC assuming a spherical particle shape.[4,20]

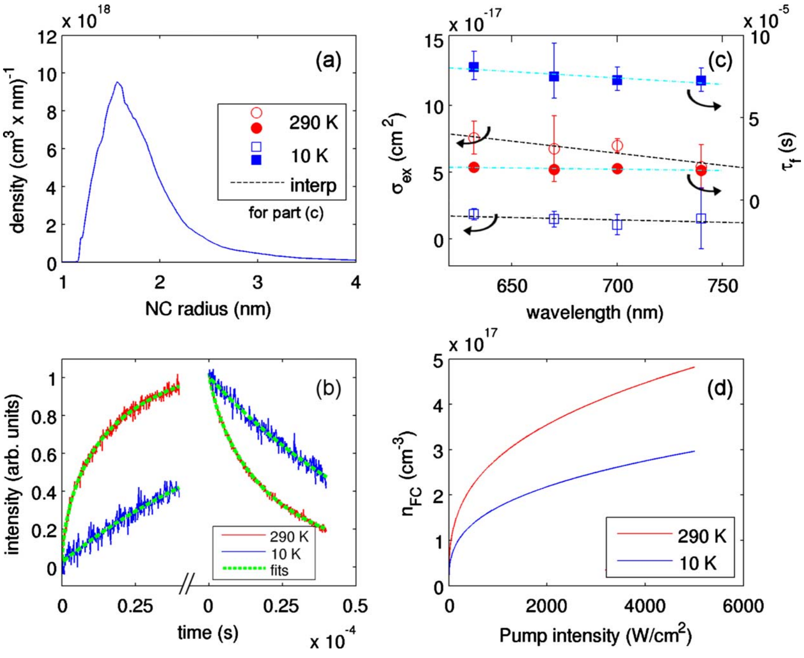

FIG. 8. (Color online) (a) The Si-NC density distribution of this sample as a function of Si-NC radius. (b) Time-resolved measurements of the Si-NC rise and fall time. Fits to extended exponential distributions yield a rise time of 17 μs and a fall time of 20 μs for the sample at 290 K, and a rise time of 78 μs and a fall time of 79 μs for the sample at 10 K. (c) The excitation cross section and the lifetimes (τ_f) of the Si-NCs as a function of emission wavelength, for both 290 and 10 K. (d) The calculated free carrier concentration as a function of pump intensity for 290 and 10 K.

Although the bulk Si Auger coefficient is used, the Auger recombination time of Si-NCs with similar sizes as the ones in this work has been observed to match well with Auger time constant found when using the bulk figure.[20] Finally, the density of free carriers at a pump flux ϕ [$n_{\mathrm{FC}}(\phi)$] can be found by integrating the occupation for NCs of all sizes[4]

$$n_{\mathrm{FC}}(\phi) = \int_R f(R,\phi)\rho(R)dR. \tag{6}$$

We plot the results in Fig. 8(d), and observe that due to the smaller excitation cross section at 10 K, the free carrier concentration at 10 K at any particular pump flux is approximately one half that of the free carrier concentration at 290 K.

Finally, this free carrier concentration can be related to the change in linewidth of the cavity modes, assuming the FCA is the dominant absorption process

$$\Delta\mathrm{FWHM} = \frac{\lambda^2\Gamma}{2\pi n_{eff}}\sigma_{\mathrm{FCA}}(\lambda)n_{\mathrm{FC}}, \tag{7}$$

where ΔFWHM is the change in the cavity linewidth, Γ is the overlap of the cavity mode with the active material, n_{eff} is the effective index of the cavity mode, and $\sigma_{\mathrm{FCA}}(\lambda)$ is the free carrier absorption cross section. We calculate n_{eff} and Γ from the FDTD simulations with various beam dimensions. We plot the change in linewidth (obtained from the power-dependence curves) against n_{FC}, and find σ_{FCA} through a linear fit to the slope [Fig. 9(a), showing data from the cavity near 720 nm] for cavities at both 290 and 10 K. In addition, we plot all of the fitted σ_{FCA} for cavities throughout the Si-NC PL spectrum at both temperatures, as a function of the cavity wavelength, in Fig. 9(b). We first note that the mean-free carrier absorption obtained in the nanobeam cavities is a factor of 4 increased from that obtained in Ref. 4 at room temperature. In addition, as seen in Fig. 9(a), the change in the cavity linewidth with increasing pump power is larger at 10 K than at 290 K for the same cavity. Even more, because the free carrier density at the same pump power is lower at 10 K than at 290 K, we calculate that the σ_{FCA} is approximately six times higher at 10 K than at 290 K [Fig. 9(b)]. While FCA in bulk crystalline materials decreases with temperature,[21] the FCA mechanism in Si-NCs of scattering at

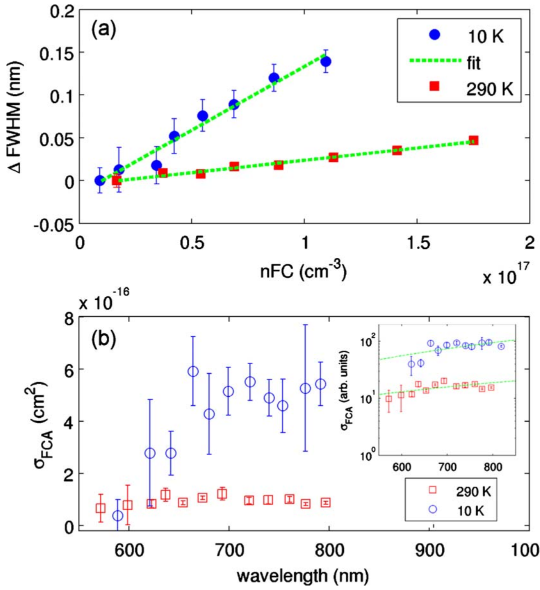

FIG. 9. (Color online) (a) The change in cavity linewidth as a function free carrier density for a representative cavity around 720 nm at 290 and 10 K. Linear fits to the data are also shown. (b) The free carrier absorption cross section (σ_{FCA}) obtained from linear fits such as those in part (a), as a function of wavelength, for different cavities throughout the PL spectrum of the Si-NCs. The inset shows the same data renormalized in a small V_m setting. The dashed lines represent fits to a λ^b model, where $b=1.3$ and 1.8 for the 290 K and 10 K data, respectively.

the Si-NC boundary[4] could be less sensitive to temperature. However, We do not observe the λ^2 dependence of σ_{FCA} generally associated with FCA,[4] especially at room temperature, where σ_{FCA} is seen to decrease with wavelength.

While the calculation above allows easy direct comparison with the figures obtained in Ref. 4, they assume that the optical mode of the cavity is traveling in an effective medium with some effective index and group velocity. While such an assumption is valid for large cavities such as μ-disks, they are oversimplified for the case of high-Q, low-V_m cavities. In the cavity setting, the Purcell enhanced strength of absorption is given by[22]

$$\gamma \propto \int_{\omega} |g_0|^2 \rho(\omega) d\omega \propto \int_{\omega} \rho(\omega)/V_m d\omega, \qquad (8)$$

where $|g_0|^2 \propto 1/V_m$ is the emitter-field interaction term, and $\rho(\omega)$ is the joint density of states associated with the electronic transition for FCA and the optical density of states of the cavity. However, since the transition for FCA is a broad continuum, the normalized narrow bandwidth optical density of states from the cavity is integrated out, resulting in no enhancement of the absorption rate in high-Q cavities. Thus, in this case, the Purcell enhanced absorption should only be proportional to Γ and the inverse of V_m. We renormalize the calculated σ_{FCA} of Fig. 9(b) with those considerations and plot the results in the inset of the same figure, along with their respective fits to a $\sigma_{\mathrm{FCA}} \propto \lambda^b$ model. We obtained $b = 1.3$ and 1.8 for the 290 K and 10 K cases, respectively, which is more consistent with FCA being the cause of the power-dependent absorption.

In conclusion, we have demonstrated high-Q nanobeam cavities in low-index Si-NC doped $\mathrm{SiO_2}$, with experimental Q as high as 9000, and mode volumes of $1.5(\lambda/n)^3$, operating in the visible wavelengths from 600 to 820 nm. We have also observed a decrease in Q factor with decreasing temperature, which is associated with enhanced absorption losses from the Si-NCs with decreasing temperature.[14] Nevertheless, high Q's were maintained for all temperatures and all wavelengths. Finally, we have also investigated the free carrier absorption mechanism associated with the pump-power-dependent linewidth broadening and computed the free carrier absorption cross section. As shown in previous work,[4] the free carrier absorption cross section in Si-NCs are much larger than the corresponding figure in bulk Si. In this work, we have shown that the absorption cross section of the Si-NCs is further increased when the NCs are placed in a high-Q, low-V_m cavity, as we demonstrate a fourfold increase in the measured cross section at room temperature. In addition, we also measure the free carrier absorption at cryogenic temperatures and find that the FCA cross section at 10 K is increased by nearly one order of magnitude from the value at room temperature. This evidence suggests that cavity enhanced absorption may be applicable to processes such as FCA, and are not limited to just emission of single quantum dots,[23] ensembles of atoms with large homogeneous broadening,[14] and even Mie scattering.[24] Even more, the large effective absorption coefficients of Si-NCs in microcavities could hamper development of a lasing source, whether the Si-NCs serve as the emitters or as the sensitizer as in Si-NCs mediated emission from Er doped SiO_x. Finally, it is likely that cooling down systems involving Si-NCs would present additional challenges. Although many nonradiative phonon-mediated recombination processes decrease with decreasing temperature, we have demonstrated that FCA increases dramatically with decreasing temperature as well, possibly offsetting some of the gains. Nevertheless, these Si-NC beams are made by fully CMOS-compatible fabrication techniques, and certainly present interesting platform for applications such as sensors, as their cavity modes have high overlap with the environment and their emission spans a wide range of wavelengths in the visible. Such cavities would also be biocompatible and could be functionalized for probing emission from molecules. Finally, the enhancement of emission could be increased by modifications in the cavity design and creating high-Q cavities in low index materials remains an interesting challenge.

The authors acknowledge the Interconnect Focus Center [one of six research centers funded under the Focus Center Research Program (FCRP), a Semiconductor Research Corporation entity], the Toshiba corporation, and the NSF (Y.G.) for funding. Fabrication was done at Stanford Nanofabrication Facilities.

---

*yiyangg@stanford.edu

[1] *Towards the First Silicon Laser*, edited by L. Pavesi, S. Gaponenko, and L. Dal Negro (Kluwer Academic, Netherlands, 2003).

[2] L. Pavesi, L. Dal Negro, C. Mazzoleni, G. Franzò, and F. Priolo, Nature (London) **408**, 440 (2000).

[3] R. D. Kekatpure and M. L. Brongersma, Phys. Rev. A **78**, 023829 (2008).

[4] R. D. Kekatpure and M. L. Brongersma, Nano Lett. **8**, 3787 (2008).

[5] P. Bianucci, X. Wang, J. G. C. Veinot, and A. Meldrum, Opt. Express **18**, 8466 (2010).

[6] M. Barth, N. Nüsse, J. Stingl, B. Löchel, and O. Benson, Appl. Phys. Lett. **93**, 021112 (2008).

[7] J. S. Foresi, P. R. Villeneuve, J. Ferrera, E. R. Thoen, G. Steinmeyer, S. Fan, J. D. Joannopoulos, L. C. Kimerling, H. I. Smith, and E. P. Ippen, Nature (London) **390**, 143 (1997).

[8] P. B. Deotare, M. W. McCutcheon, I. W. Frank, M. Khan, and M. Lončar, Appl. Phys. Lett. **94**, 121106 (2009).

[9] M. Eichenfield, R. Camacho, J. Chan, K. J. Vahala, and O. Painter, Nature (London) **459**, 550 (2009).

[10] M. W. McCutcheon and M. Lončar, Opt. Express **16**, 19136 (2008).

[11] Y. Gong and J. Vučković, Appl. Phys. Lett. **96**, 031107 (2010).

[12] J. Chan, M. Eichenfield, R. Camacho, and O. Painter, Opt. Express **17**, 3802 (2009).

[13] H. Rinnert, O. Jambois, and M. Vergnat, J. Appl. Phys. **106**, 023501 (2009).

[14] Y. Gong, M. Makarova, S. Yerci, R. Li, M. J. Stevens, B. Baek, S. W. Nam, R. H. Hadfield, S. N. Dorenbos, V. Zwiller, J. Vučković, and L. Dal Negro, Opt. Express **18**, 2601 (2010).

[15] I. Sychugov, R. Juhasz, J. Valenta, and J. Linnros, Phys. Rev. Lett. **94**, 087405 (2005).

[16] S. G. Johnson, M. Ibanescu, M. Skorobogatiy, O. Weisberg, J. D. Joannopoulos, and Y. Fink, Phys. Rev. E **65**, 066611 (2002).

[17] L.-D. Haret, T. Tanabe, E. Kuramochi, and M. Notomi, Opt. Express **17**, 21108 (2009).

[18] L.-W. Wang and A. Zunger, Phys. Rev. Lett. **73**, 1039 (1994).

[19] L. Pavesi and M. Ceschini, Phys. Rev. B **48**, 17625 (1993).

[20] F. Trojánek, K. Neudert, M. Bittner, and P. Malý, Phys. Rev. B **72**, 075365 (2005).

[21] K. G. Svantesson and N. G. Nilssm, J. Phys. C **12**, 3837 (1979).

[22] J. J. Sakurai, in *Modern Quantum Mechanics*, rev. ed., edited by S. F. Tuan (Addison-Wesley, Reading, 1994).

[23] D. Englund, D. Fattal, E. Waks, G. Solomon, B. Zhang, T. Nakaoka, Y. Arakawa, Y. Yamamoto, and J. Vučković, Phys. Rev. Lett. **95**, 013904 (2005).

[24] T. J. Kippenberg, A. L. Tchebotareva, J. Kalkman, A. Polman, and K. J. Vahala, Phys. Rev. Lett. **103**, 027406 (2009).